Modeling of DC-Side Dynamics in PV/Battery Grid-forming Inverter Systems

Xi Luo
School of Electronics and Computer Science
University of Southampton
Southampton, U.K.
xi.luo@soton.ac.uk

Alexandros G. Paspatis
School of Electrical and Computer Engineering
National Technical University of Athens
Athens, Greece
agpaspatis@mail.ntua.gr

Abhinav Kumar Singh
School of Electronics and Computer Science
University of Southampton
Southampton, U.K.
a.k.singh@soton.ac.uk

Nikolaos Hatziargyriou
School of Electrical and Computer Engineering
National Technical University of Athens
Athens, Greece
nh@power.ece.ntua.gr

Efstratios I. Batzelis
School of Electronics and Computer Science
University of Southampton
Southampton, U.K.
e.batzelis@soton.ac.uk

***Abstract*—The DC-side dynamics of two-stage grid-forming (GFM) inverters are often neglected or oversimplified in power system studies, although they play a vital role in stability. Detailed models for the primary source and power converter are not practical for complexity reasons, leading usually to DC side representations that omit critical aspects such as the operational limits. To bridge this gap between accuracy and simplicity, this paper proposes for the first time an equivalent model for the DC side dynamics of GFM systems that captures all important dynamics and limits in a simple formulation. The model supports either batteries or photovoltaic arrays as a primary source and is easily parameterizable with minimal information, thus proving a useful tool for grid stability studies. Time-domain simulations validate the proposed equivalent model.**

Keywords—DC-Side dynamics, grid-forming, solar photovoltaic (PV), maximum power point, battery, state of charge.

I. Introduction

Through the advancements in power electronics, the energy paradigm is changing from fossil fuel-powered generation to renewable energy resources (RESs), such as solar and wind, leading to an inverter-dominated grid. Inverters have been typically operating in *grid-following* (GFL) mode, acting as current sources to deliver active and reactive power from the DC-side to the AC network. However, their synchronization mechanism through a phase-locked loop (PLL) is proven unstable at weak grid conditions, negatively impacting the stability of high-RES systems [1]. The *grid-forming* (GFM) inverter has emerged lately as a promising alternative, acting as a voltage source and being capable of forming its own frequency and voltage outputs. It is now acknowledged that GFM are superior to GFL inverters in terms of grid support and stability in weak grids [1], [2].

The majority of research on GFM inverters assumes a single DC/AC conversion stage that regards the DC side as an ideal voltage source [3]. However, in practice, the primary sources are often equipped with a front-end converter for the DC-link voltage regulation. In [2], a two-stage grid-connected PV system comprising a DC/DC converter and GFM inverter is explored with a focus on meeting the power and current operational limits. It was suggested in [4] that insufficiently fast dynamic response from the primary side may cause interactions with the inverter and adversely affect system stability. Proper modeling of the DC-side dynamics in the two-stage system thus becomes essential. This paper explores this topic for batteries or photovoltaic (PV) inputs, which exhibit certain similarities in the DC/DC converter.

The full picture on the DC side can be captured via the detailed *switching model* that incorporates all circuit details. However, representing the high-frequency switching phenomena entail high computational complexity, without conveying any significant information on control-driven and grid-related dynamics. This is why *average-value models* have been traditionally used in power electronics for control design and simulations over longer timescales [5]. Still, parametrizing such models require lots of input data, such as the DC/DC converter's input capacitor and inductance, normally not available in power system studies.

This is why in such analyses the DC-side dynamics are represented via simplified *equivalent models*, usually comprising a current source for the primary input and a DC link capacitor, as well as some control functions [4]–[6]. The dynamics of the primary source are modelled through a first-order low pass filter (LPF) in [7], [8], while in [4] the outer voltage control loop is also considered for a battery-based GFM system. However, the aspect of operational limits has been neglected in these studies. Authors in [5] emphasize that (i) the capacity of PV panels is limited by their maximum power generation; and (ii) batteries are also limited by their State of Charge (SoC) in view of long-term safety and longevity. In [8], [9], these limits are mentioned, but details on how they are applied and modelled are missing. In addition, most of these models require input data not readily available, such as the time constant of the first-order LPF.

To address these challenges, this paper introduces an equivalent model for the DC-side dynamics of PV- or battery-based GFM systems that bridges the gap among accuracy, simplicity and parametrization. The proposed model delivers accuracy comparable to circuit-based alternatives, but is simple to implement and parameterize, thus rendering a useful tool in power system studies. The key novelties are:

- Fully considering and modeling the operational limits of the primary source and DC/DC converter;
- Simplifying some dynamics via a first-order LPF, whose time constant is easily attainable;
- Capturing the power losses by means of a shunt resistance, which again is readily found.

II. Modelling of the Primary Source

Prior to discussing the DC-side modeling method, the considerations of the primary source are first outlined, to guide the analysis that follows. In this study, PV systems and

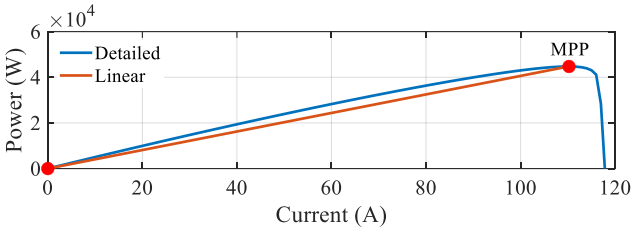

Fig. 1. Power–current characteristic curve of a PV array at STC.

Battery Energy Storage Systems (BESS) are the focal points.

A. The PV Generator

The power-current (P–I) characteristic curve of a typical PV array is depicted in blue in Fig. 1. Since the PV array is neither a voltage nor a current source, the power output varies with the operating point up to the maximum power point (MPP). Several circuit-based models have been proposed to accurately simulate the performance of PV modules, one representative of which is the five-parameter model described in [10]. However, such a detailed approach would be too complex for our target application; alternatively, this paper considers a linear approximation of the *P–I* characteristic in the voltage source region as the red line indicates in Fig. 1. The slope of that characteristic is $P_{mp}/I_{mp}=V_{mp}$, which implies that the PV array is treated as a constant voltage source V_{mp}. This simplification is based on the limited PV voltage variation at that region [11], which is shown later that delivers a good compromise between accuracy and simplicity.

With the proposed linear approximation, the sole calculation required refers to the MPP voltage and current, which are readily found via the method described in [12]. The input data are (i) the operating conditions: irradiance G (normalized) and cell temperature T (in Kelvin; $\Delta T = T - T_0$; $\lambda T = T/T_0$); and (ii) to nominal PV array attributes available in the datasheet: MPP current and voltage at standard test conditions (STC), I_{mp0}, V_{mp0}, open circuit voltage V_{oc0}, and temperature coefficient $\alpha_{I_{sc}}$and $\beta_{V_{oc}}$.

According to [12], the MPP coordinates are given by

$$I_{mp} = G \cdot I_{mp0}\left(1 + \alpha_{I_{mp}}\Delta T\right) \quad (1)$$

$$V_{mp} = V_{mp0}[1 + \varepsilon_0 \lambda T ln G + \varepsilon_1(1 - G) + \beta_{V_{mp}}\Delta T] \quad (2)$$

where $\alpha_{I_{mp}}$and $\beta_{V_{mp}}$ are normalized temperature coefficients of the MPP current and voltage; ε_0 and ε_1 are the irradiance factors of the MPP voltage. These parameters are explicitly calculated via the following equations

$$\alpha_{I_{mp}} = \alpha_{I_{sc}} + (\beta_{V_{oc}} - 1/T_0)/(w_0 - 1) \quad (3)$$

$$\beta_{V_{mp}} = \frac{V_{oc0}}{V_{mp0}}\left[\frac{\beta_{V_{oc}}}{1+\delta_0} + \frac{\delta_0(w_0-1)-1/(1+\delta_0)}{T_0}\right] \quad (4)$$

$$\varepsilon_0 = \frac{\delta_0}{1+\delta_0}\frac{V_{oc0}}{V_{mp0}},\ \varepsilon_1 = \delta_0(w_0 - 1)\frac{V_{oc0}}{V_{mp0}} - 1. \quad (5)$$

where δ_0 and w_0 are auxiliary parameters given by

$$\delta_0 = \frac{1-\beta_{V_{oc}}T_0}{50.1-\alpha_{I_{sc}}T_0},\ w_0 = W\left\{e^{\frac{1}{\delta_0}+1}\right\} \quad (6)$$

where W{.} is the Lambert W function evaluated in this paper via the approximation formula given in [12]. Applying (1)-(6) leads to the MPP power $P_{mp} = V_{mp} \cdot I_{mp}$.

B. The Battery Source

The main limitations of a battery-based DC-side in GFM inverters relate to the power (current) limitation and the SoC (energy) limitation. In fact, SoC is a parameter that reflects the energy stored in the battery, which is calculated by

$$SoC(\%) = SoC_0 - \frac{1}{Q}\int_0^t i(t)\,dt \quad (7)$$

where SoC_0 is the initial SoC; and Q is the nominal capacity (in Ah). Thus, the maximum SoC is at 100% fully charged; and the minimum is at 0% empty. Usually, operation in the range of 10%-90% is required for degradation reasons; this introduces the *energy limit*. It is noteworthy that within that range, the battery is usually modelled in the literature as an ideal voltage source [13], an assumption also adopted here.

However, there is also a *power limit* referring to the current rating of the battery bank and DC/DC converter, usually given as a single value for the entire battery energy storage system (BESS) [14]. The aforementioned limitations can be compiled to the operational range $[I_{slim,min}, I_{slim,max}]$ of the input current of the front-end converter in GFM systems as follows

$$I_{slim,max} = min\,(I_{rated}, I_{soc}^{lim+}) \quad (8)$$

$$I_{slim,min} = max(-I_{rated}, I_{soc}^{lim-}), \quad (9)$$

where I_{soc}^{lim+} is 0 when SoC drops below 10% and I_{rated} otherwise. Similarly, I_{soc}^{lim-} is 0 when SoC rises above 90% and $-I_{rated}$ otherwise, with I_{rated} being the rated (maximum) current of the BESS. These limits are enforced by appropriate control functions [15], as explained below.

III. Modelling of DS-Side Dynamics in GFM Inverters

In this section, the modelling of the DC-side dynamics of GFM inverters is discussed, starting from the well-known switching and average-value modelling approaches, and eventually introducing the proposed equivalent model.

A. Switching Model

The full picture of inverter's DC side is given by the detailed switching circuit model. Fig. 2(a) shows the DC-side of PV and battery systems consisting of the primary source, inductor (L_{conv}), switch(es) and diode, as well as input and output capacitors (C_{pv}, and C_{dc}). Please note the similarities between the two systems. The control scheme of these converters is common (see Fig. 2(b)), featuring typically (i) an outer voltage loop to regulate the DC link voltage and (ii) an inner current loop to control the input current by adjusting the duty cycle *d*.

Current-limiting is accomplished using a clamping anti-windup scheme that ensures the output reference current can be saturated within the designated range. For a PV system, the operating current is inherently limited to the current at MPP I_{mp} assuming voltage-source operation, which is commonly adopted in PV GFM systems [2]. The current-limit range for batteries is determined by SoC and current rating from (8)-(9). It is worth emphasizing that the switching model represents the ground truth but is not practical for power system studies. It is used hereby only as benchmark for accuracy.

B. Average-Value Model

The average-value model provides a simpler simulation approach, usually adopted in control design. The switching networks are replaced by equivalent voltage and current sources, as shown in Fig. 3 for the study-case system (assuming continuous conduction mode – CMM). The control scheme of Fig. 2 remains the same. Still, the level of detail in this model is too much for power system studies, requiring

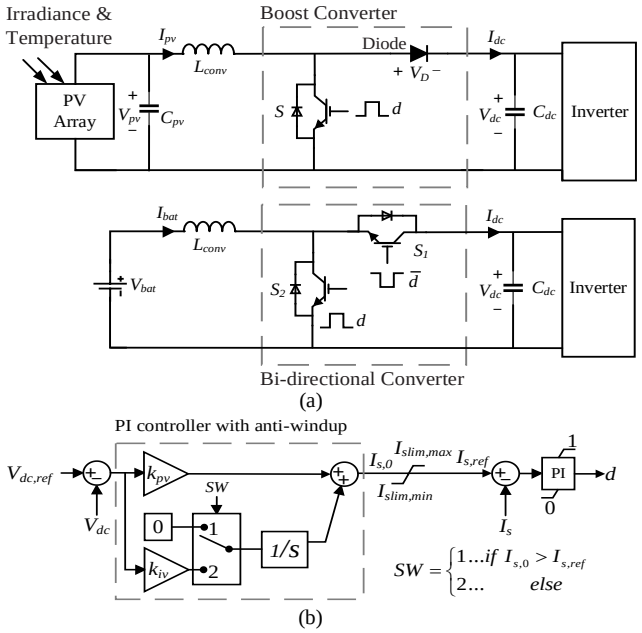

Fig. 2. Switching model configuration (a) converter topology for PV (upper) and battery (lower) systems, (b) converter control loop.

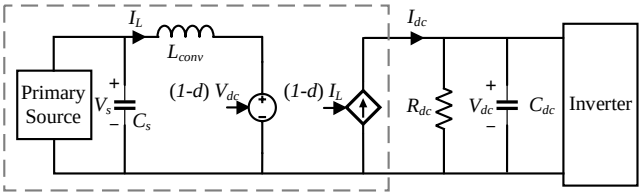

Fig. 3. Average-value model configuration.

information such as the converter's input capacitance or inductance normally not known at the higher system level.

C. Proposed Equivalent Model

To allow for simpler representation of the DC-side dynamics of GFM inverters in system-level studies, an equivalent model is developed in this section which is based on the average-value model but with less input data. Fig. 4 shows that model, consisting of a controllable current source for the system's input, a shunt resistance for the power losses and the DC link capacitor. The model retains the outer voltage loop that sets the input reference current $I_{s,ref}$ as in Fig. 2, but simplifies the cascaded current controller (Fig. 2(b)) and DC/DC converter (Fig. 3) to a first-order LPF and a gain. This approach preserves the important dynamics, but at a rather abstract level that is more easily parameterizable.

The parameters of this model are (i) the DC link capacity C_{dc} and reference voltage V_{ref}, and the PI controller gains k_{pv}, k_{iv}, as well as (ii) the primary source voltage V_s, parasitic shut resistance R_{dc}, input current limits $I_{slim,max}$ and $I_{slim,min}$ and the time constant τ. The former parameters are usually known in power system studies, while the latter can be found as explained in the following.

1) Primary Source Representation

The primary source is effectively represented via a constant voltage source V_s for both PV and battery cases, being equal to V_{mp} or V_{bat} respectively (see Section II). The former can be easily calculated via (2)-(6), while the latter is the battery rated voltage. The current limits $I_{slim,max}$ and $I_{slim,min}$ are found via the primary source constraints (MPP current for PV, SoC limit for battery) and the DC/DC converter rating.

TABLE I. PRIMARY SOURCE PARAMETERS

Source	*Inputs*	V_s	$I_{slim,min}$	$I_{slim,max}$
PV	G, T, I_{mp0}, V_{mp0} V_{oc0}, α_{Isc}, β_{Voc}	V_{mp}	0	$min\ (I_{rated}, I_{mp})$
Battery	SoC	V_{bat}	$max(-I_{rated}, I_{soc}^{lim-})$	$min\ (I_{rated}, I_{soc}^{lim+})$

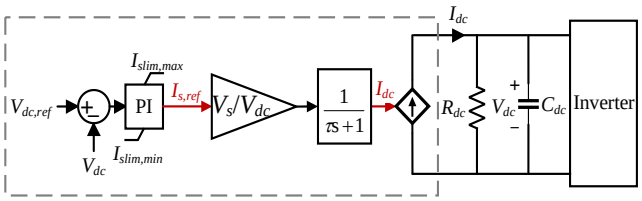

Fig. 4. Proposed equivalent model, including circuit and control.

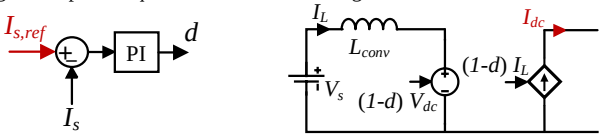

Fig . 5. Current control-to-DC current system model.

These points are concisely captured in Table I for ease of reference.

2) Shunt Resistance Rdc

The power conversion from the primary source to the DC side suffers from power losses at hardware components. For the purposes of this model, this can be simply represented by a shunt resistance R_{dc} across the terminals of DC link. Although such an approach is adopted in [4], [9] as well, it is not explained how that equivalent R_{dc} should be calculated. This paper employs the DC/DC converter efficiency η (always known or assumed) to relate the power losses to R_{dc} as in

$$\eta = P_{out} / P_{in}\,,\ R_{dc} = v_{dc}^2/((1-\eta)\cdot P_{in}). \tag{10}$$

Normally the power losses vary with the power and current levels, so a fixed resistance value through (10) is certainly another simplification; yet, it is shown later that it is acceptable for this model.

3) Time Constant τ

The equivalent model simplifies the high-bandwidth inner current control loop and the primary source circuit to a simple first-order LPF (a time delay) with a time constant τ. Similar approaches have been adopted in [8], but without justifying the scientific basis or quantifying τ. This gap is met in this paper by means of small-signal analysis. Given that both PV and battery inputs are treated as a constant voltage source V_s (see Section II), the input capacitor C_s can be neglected in Fig. 3, and the input current I_s coincides with the inductor current I_L. Deriving the current control-to-DC current (Fig. 5) transfer function $H(s)$ that relates the input current reference $I_{s,ref}$ to the output current I_{dc} yields

$$H(s) = \frac{\hat{I}_{dc}}{\hat{I}_{s,ref}} = \frac{-I_L k_p s^2 + \left(\frac{V_{dc}}{L}(1-D)k_p - I_L k_i\right)s + \frac{V_{dc}}{L}(1-D)k_i}{s^2 + \frac{V_{dc}}{L}k_p s + \frac{V_{dc}}{L}k_i} \tag{11}$$

where $\hat{I}_{s,ref}$ denotes the incremental reference input current generated from the voltage controller, $\hat{I}_{dc}$ the incremental DC current, I_L and D the steady-state inductor current and duty cycle, L and V_{dc} the inductance and nominal DC-link voltage, k_p and k_i the current PI controller gains.

Analyzing (11) reveals that the transfer function has two pairs of poles p_1, p_2 and zeros z_1, z_2, among which (z_1, p_1) lie at low frequencies and are close to zero, which means that their dynamic characteristics cancel each other out. Hence, the

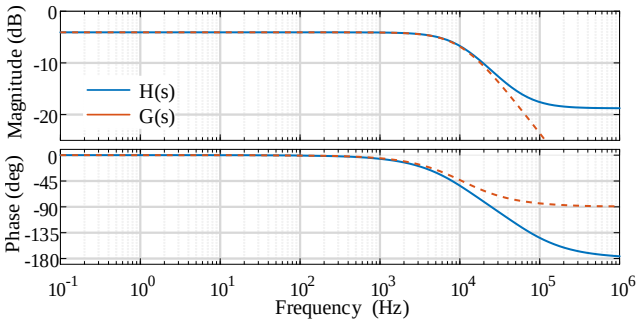

Fig. 6. Bode plot of transfer function and designed LPF.

TABLE II. SYSTEM SPECIFICATIONS

Components	*Value*
PV array	P_{mp0} = 44.8 kW; V_{mp0}= 406 V; I_{mp0}= 110.25 A at STC; R_{dc}= 204.08 Ω; η = 93%; I_{rated}= 112.66 A; k_{pv} = 1; k_{iv} = 50; k_{pi} = 0.02; k_{ii} = 0.1; τ = 0.0942 ms;
Batteries	V_{bat} = 450 V; R_{dc} = 1262 Ω; η = 99%; I_{rated} = 112.66 A; k_{pv} = 1; k_{iv} = 50; k_{pi} = 0.02; k_{ii} = 0.1; τ = 0.0942 s
DC/DC converter	V_{dc}= 800 V; fs = 20 kHz; L = 240 uH; C_s = 370 uF; C_{dc} = 2.5 mF; I_{rated} = 112.66 A;

system is mainly influenced by the remaining pole p_2 and zero z_2, as shown in the Bode plots of Fig. 6. Furthermore, it is found that z_2 lies at several hundred kHz, a frequency that does not affect control or grid related dynamics. Therefore, it is reasonable to approximate $H(s)$ solely via p_2, which essentially represents a first-order LPF

$$G(s) = A\frac{1}{\frac{s}{\omega_0}+1} = \frac{V_s}{V_{dc}}\frac{1}{\frac{s}{k_p \cdot V_{dc}/L}+1} \tag{12}$$

Here, $A = H(0) = 1 - D = V_s/V_{dc}$ ($V_s = V_{mp}$ or V_{bat}) is the dc gain of the filter, $\omega_0 = p_2 \approx k_p(V_{dc}/L)$ is the cut-off frequency, and thus the time constant is given by

$$\tau = \frac{L}{k_p V_{dc}}. \tag{13}$$

As expected, Fig. 6 shows that this approximation matches well with the system dynamics within a few kHz in both magnitude and phase. To apply (13), one needs the current controller gain k_p, inductance L and DC-link voltage V_{dc}; in case of missing data, a time constant from a few ms to fractions of ms is a reasonable assumption.

IV. VALIDATION

In order to evaluate the effectiveness of the proposed model, three case studies are presented in this section assuming PV and battery inputs. The equivalent model (*Eq*) is compared to a conventional simplified model that neglects the operational limits [4] (*Eq:nolim*) and assessed over the switching (*Sw*) and average-value (*Ave*) benchmark models. The inverter-side is modelled as a variable current source for simplicity which suffices for this investigation. The parameters of system components are given in Table II.

A. PV Irradiance Change

In this case, the PV irradiance changes from 600 to 300 W/m^2 at a rate of 100 Wm^{-2}s^{-1} which is quite high [2] and recovers within a few seconds, with the results reflected in the values of I_{mp} in Fig. 7 (blue dotted lines). The inverter-side current is set to a constant value of 20 A. When the irradiance drops too low (from 4 to 6 s), the PV array cannot support the load which is reflected in the DC link voltage in Fig. 7.

The Ave model (yellow lines) presents a similar dynamic response to Sw as expected, with the high-frequency

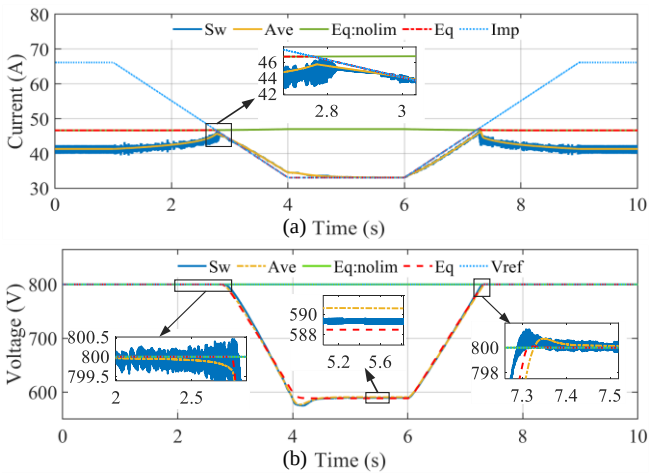

Fig. 7. (a) PV current and (b) DC-link voltage in the case of an irradiance change .

TABLE III. ACCURACY AND COMPLEXITY COMPARISON OF CASES A & B

Type of model	*Case A*			*Case B*		
	Max	*RMSE*	*Time*	*Max*	*RMSE*	*Time*
Sw	Benchmark		436.2s	Benchmark		66.2s
Ave	0.96%	0.21%	182.1s	0.34%	0.09%	33.2s
Eq:nolim	39.27%	13.00%	7.1s	13.87%	4.54%	1.4s
Eq	2.72%	0.39%	9.4s	0.59%	0.13%	1.5s

switching ripple only missing. The introduced Eq model (red lines) can effectively represent the system dynamics, where the voltage results sufficiently match the variations of the Ave and Sw benchmarks. Here limited steady-state voltage deviations 4-6 s are due to the power losses simplification via R_{dc}. It is worth noting that although the PV current in Eq is higher than Sw and Ave at high irradiance because of the linear approximation of the PV source, this is not manifested as any V_{dc} deviation. What really matters is apparently the current limit representation, which comes into picture at low irradiance to accurately reflect the V_{dc} drop with Eq. This is where the conventional Eq-nolim (green lines) fails, not capturing the voltage deviation, which proves the importance of considering the operational limits in DC-side dynamics. Table III further calculates the maximum deviation and root-mean-square error (RMSE) based on the Sw DC-link voltage results and summarizes the execution time. It reveals that the simplified Eq model delivers accuracy very close to Ave but at a computational cost similar to Eq:nolim, thus effectively striking the right balance between complexity and accuracy.

B. Inverter-side Current Change in PV System

The inverter-side current is changed in this scenario at t = 0.1 s, 0.4 s, 0.7 s and 0.9 s, in successive steps from 20 A to 30 A, 40 A, 60 A and finally down to 20 A. The incident irradiance is set to STC conditions. The results of Fig. 8 demonstrate that Eq matches very well the Sw and Ave benchmarks in terms of DC link voltage and power, and that the overestimation of PV current is not really transferred to the DC link and AC sides. This confirms that Eq captures nicely both minor fluctuations and major sags in DC link voltage accurately, which is the major purpose of such a model. In contrast, the conventional Eq-nolim fails to consider the current limit during 0.7-0.9 s which results in severe misrepresentation of the DC link voltage at that time. In Table III, the superiority of the Eq model is verified again from the perspectives of accuracy and computational complexity.

C. Inverter-side Current Change in Battery System

Similar to the previous subsection, an inverter-side current

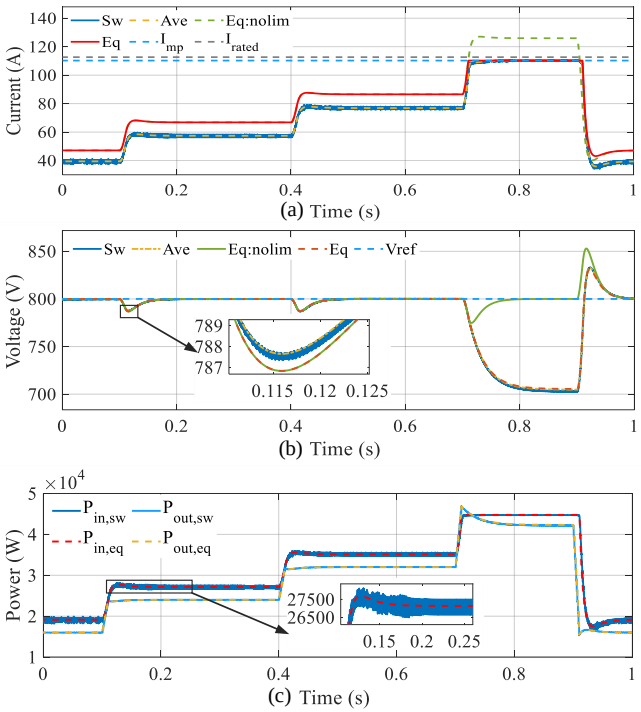

Fig. 8. (a) PV current, (b) DC-link voltage, and (c) converter power in the case of inverter-side current change.

change is considered for the battery system to highlight the applicability of the proposed equivalent model. In the results of Fig. 9, the inverter-side current changes occur at t = 0.1 s, 0.3 s, 0.5 s, 0.7 s, 0.8 s and 0.82 s ranging from 0 A to 50 A, 25 A, 0 A, -40 A, -80 A, -40 A. Particularly the requirement for -80A inverter-side current during 0.8-0.82 s, triggers the input current limitation, proving the capability of Eq to accurately representing the DC dynamics at any conditions. This is clearly not the case for the Eq-nolim model, which misses an important voltage fluctuation during 0.8-0.82 s.

V. CONCLUSION

The goal of this study is to provide a model and methodology to represent the DC-side dynamics of PV/battery GFM systems in a simple manner yet accurate manner at any conditions. The proposed scheme avoids many circuit details in the DC-side circuit, retaining the absolutely necessary circuit and control elements. Thus, users need only to define a limited number of parameters that are readily available or derived in power system studies. The validity of the equivalent model is verified via three case studies and compared with an existing approach in the literature. The results reveal that the proposed model retains the important DC-side dynamics at a simple formulation, in contrast to complex switching models or oversimplified equivalent alternatives. Future work could include extension of this model for wind primary source and an evaluation of the grid-wide stability benefit of accurate DC-side dynamics modeling in inverter-intensive power systems.

ACKNOWLEDGMENT

This work was supported by the European Union's Horizon 2020 Research and Innovation Program and the Department of Science and Technology (DST), India through the RE-EMPOWERED Project under Grant agreement no. 101018420, DST/TMD/INDIA/EU/ILES/2020/50(c), respectively, and the Royal Academy of Engineering under the Engineering for Development Research Fellowship scheme (no. RF\201819\18\86).

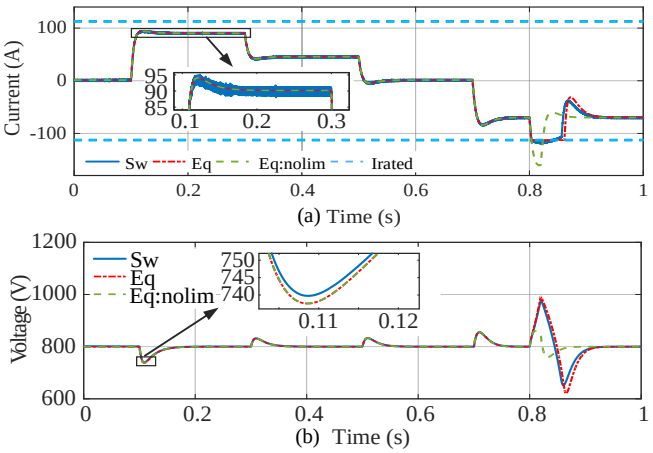

Fig. 9. (a) Battery current and (b) DC-link voltage in the case of an irradiance change.

REFERENCES

[1] R. H. Lasseter, Z. Chen, and D. Pattabiraman, "Grid-Forming Inverters: A Critical Asset for the Power Grid," *IEEE J. Emerg. Sel. Top. Power Electron.*, vol. 8, no. 2, pp. 925–935, Jun. 2020.

[2] B. Pawar, E. I. Batzelis, S. Chakrabarti, and B. C. Pal, "Grid-Forming Control for Solar PV Systems With Power Reserves," *IEEE Trans. Sustain. Energy*, vol. 12, no. 4, pp. 1947–1959, Oct. 2021.

[3] T. Liu and X. Wang, "Transient Stability of Single-Loop Voltage-Magnitude Controlled Grid-Forming Converters," *IEEE Trans. Power Electron.*, vol. 36, no. 6, pp. 6158–6162, Jun. 2021.

[4] B. Wang and G. Verbič, "Stability Analysis of Low-Voltage Distribution Feeders Operated as Islanded Microgrids," *IEEE Trans. Smart Grid*, vol. 12, no. 6, pp. 4681–4689, Nov. 2021.

[5] J. L. R. Amenedo, S. A. Gómez, J. Alonso-Martinez, and M. G. De Armas, "Grid-Forming Converters Control Based on the Reactive Power Synchronization Method for Renewable Power Plants," *IEEE Access*, vol. 9, pp. 67989–68007, 2021.

[6] A. A. A. Radwan, Y. A.-R. I. Mohamed, and E. F. El-Saadany, "Assessment and performance evaluation of DC-side interactions of voltage-source inverters interfacing renewable energy systems," *Sustain. Energy Grids Netw.*, vol. 1, pp. 28–44, Mar. 2015.

[7] N. Sockeel, J. Gafford, B. Papari, and M. Mazzola, "Virtual Inertia Emulator-Based Model Predictive Control for Grid Frequency Regulation Considering High Penetration of Inverter-Based Energy Storage System," *IEEE Trans. Sustain. Energy*, vol. 11, no. 4, pp. 2932–2939, Oct. 2020.

[8] P. H. Divshali, A. Alimardani, S. H. Hosseinian, and M. Abedi, "Decentralized Cooperative Control Strategy of Microsources for Stabilizing Autonomous VSC-Based Microgrids," *IEEE Trans. Power Syst.*, vol. 27, no. 4, pp. 1949–1959, Nov. 2012.

[9] S. Samanta and N. R. Chaudhuri, "Stability Analysis of Grid-Forming Converters Under DC-Side Current Limitation in Primary Frequency Response Regime," *IEEE Trans. Power Syst.*, vol. 37, no. 4, pp. 3077–3091, Jul. 2022.

[10] J. Bai, S. Liu, Y. Hao, Z. Zhang, M. Jiang, and Y. Zhang, "Development of a new compound method to extract the five parameters of PV modules," *Energy Convers. Manag.*, vol. 79, pp. 294–303, Mar. 2014.

[11] L. Nousiainen *et al.*, "Photovoltaic Generator as an Input Source for Power Electronic Converters," *IEEE Trans. Power Electron.*, vol. 28, no. 6, pp. 3028–3038, Jun. 2013.

[12] E. I. Batzelis, "Simple PV Performance Equations Theoretically Well Founded on the Single-Diode Model," *IEEE J. Photovolt.*, vol. 7, no. 5, pp. 1400–1409, Sep. 2017.

[13] C. Sinkaram, K. Rajakumar, and V. Asirvadam, "Modeling battery management system using the lithium-ion battery," in *2012 IEEE International Conference on Control System, Computing and Engineering*, Nov. 2012, pp. 50–55.

[14] C. Xiang, Y. Wang, S. Hu, and W. Wang, "A New Topology and Control Strategy for a Hybrid Battery-Ultracapacitor Energy Storage System," *Energies*, vol. 7, no. 5, Art. no. 5, May 2014.

[15] F. Calero, C. A. Cañizares, and K. Bhattacharya, "Dynamic Modeling of Battery Energy Storage and Applications in Transmission Systems," *IEEE Trans. Smart Grid*, vol. 12, no. 1, pp. 589–598, Jan. 2021.